Bayesian Classification of Surface-Based Ice-Radar Images

HEMA A. MURTHY AND SIMON HAYKIN, FELLOW, IEEE

Abstract—**This paper deals with the application of the Bayes classification procedure to discriminate types of sea ice based on images obtained from surface-based marine radars. The data sets were digitized images obtained from a dual-polarized *Ku*-band radar (16 GHz) and a like-polarized *S*-band radar (3 GHz) at a site located on the northern tip of Baffin Island, Canada. The images were first range-compensated, and statistical properties of different ice types were then determined. The observed histograms for different ice types were approximated by continuous density functions. The images were classified by maximizing the *a posteriori* probabilities obtained from Bayes's rule.**

The results reported herein suggest that there is sufficient information in the reflectivity to classify the different forms of ice using decision-theoretic pattern recognition techniques.

I. Introduction

A SURFACE-BASED marine radar can be used specifically for two different purposes, namely, iceberg detection and imaging the surface features of ice.

Considerable research [1]–[10] has been done on the study of the backscatter from sea ice using airborne synthetic aperture radars (SAR's), but surface-based imaging of sea ice has received very little attention. In fact, [11] represents the first systematic research aimed at improving the performance of surface-based marine radars for ice surveillance.

The "reflectivity" of different ice types is known to depend on certain physical characteristics of the ice types. Hence, it seems worth while to employ a pattern-recognition approach to classify the different forms of sea ice. As different ice types cannot be identified by either definite shapes or sizes that are immediately evident, the application of decision-theoretic methods, rather than syntactic methods, seems more appropriate to solve the ice classification problem.

This paper first briefly discusses the data sets used in the study. The theory involved in the training of the Bayes classifier is then developed, followed by a discussion of the classification results obtained.

II. Data Sets

The data sets used for the study were obtained from field experiments conducted by the Communications Research Laboratory (CRL), McMaster University, in collaboration with the Department of Fisheries and Oceans (DFO), Canada at a site located on the northern tip of Baffin Island. Five different experimental radars were used, out of which the data obtained from the *Ku* band (both like and cross polarization) and *S* band (only like polarization) were used in the study reported herein. The analog video output of the radars were digitized to 8 bits at 9 MHz. All the images were obtained in *B*-Scan format (i.e., azimuth versus range). Aerial photographs were obtained to perform ground-truthing. The ice types on the aerial photographs were identified by ice experts at the field.

III. Some Preliminaries

Suppose (Ω, A, P) is an arbitrary probability space, where Ω is the sample space, A is a class of sets of Ω, closed under all countable set operations, where elements of A are called events, and P is the probability measure defined on A. Let B be an event in the sample space Ω. Suppose, $A_1, A_2, \cdots, A_M$ partition the sample space Ω. Given that $P(A_i) > 0$ for all i, then the conditional probability of A_i given B is defined by

$$P(A_i|B) = \frac{P(B|A_i)P(A_i)}{\sum_{i=1}^{M} P(B|A_i)P(A_i)}. \quad (1)$$

In the problem of ice classification, A_i corresponds to the different ice types that occur in an ice field, and B corresponds to the feature vector of an unknown pixel "x." $P(B|A_i)$ simply describes the probability of an event B belonging to class A_i. $P(A_i)$ represents the probability of occurrence of class A_i in the field of interest. The $P(B|A_i)$ for all i are obtained by approximating the observed histograms for different ice types by continuous density functions. $P(A_i)$ was assumed to be equal for all classes, that is, $P(A_i) = 1/M$ where M is the total number of classes. Classification is performed by maximizing the *a posteriori* probability obtained in (1). This is the Bayes rule for optimal classification. In the ice classification problem, the feature vector is one dimensional, and the feature being measured is "reflectivity."

Fig. 1 shows the block diagram of the Bayes classifier, where d_i represents the discriminant function. Specifically, we have $d_i = p(x|w_i)$, where $p(x|w_i)$ is the probability that a pixel with feature vector x belongs to class w_i.

The classifier was built to take care of situations where one class may have a bounded density function and the other may have an unbounded density function. This would require the evaluation of the probability over an infinitesimal width for an

Manuscript received October 1, 1986; revised April 22, 1987. This work was supported by the Natural Sciences and Engineering Research Council of Canada.

H. A. Murthy is with the Indian Institute of Technology, Madras 600 036, India.

S. Haykin is with the Communications Research Laboratory, McMaster University, Hamilton, Ont., Canada L8S 4K1.

IEEE Log Number 8718745.

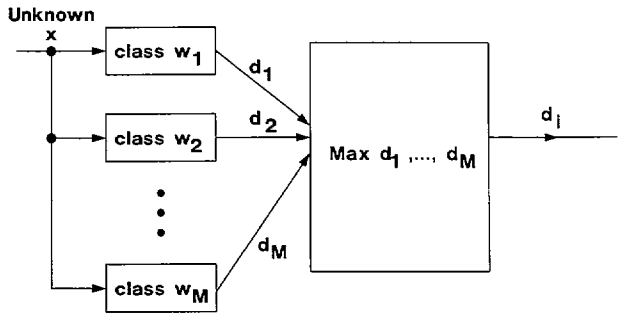

Fig. 1. $d_1 = p(x|w_1)$, $d_2 = p(x|w_2)$, $\cdots$, $d_M = p(x|w_M)$. d_i is the discriminant function for class w_i, $i = 1, 2, \cdots, M$.

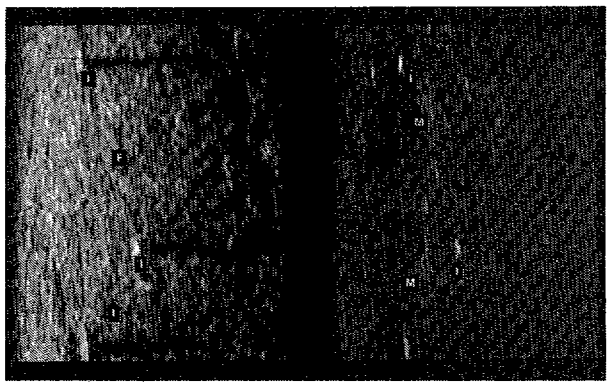

(a)

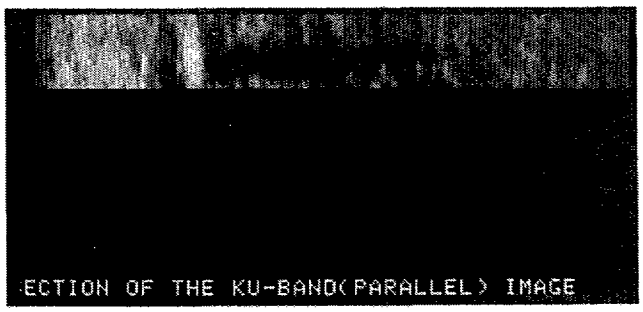

(b)

Fig. 2. (a) Section of the original *Ku*-band like-polarized and cross-polarized images: I = icebergs, M = multiyear ice, and F = first-year ice. (b) Enlarged picture of iceberg followed by a shadow.

unambiguous decision at the class boundary, hence the use of conditional probabilities in (1).

IV. Parametric Training of the Bayes Classifier

Parametric training of the Bayes classifier involves two steps: sample collection and estimation of unknown distribution parameters. These two steps are described in the sequel.

A. Sample Collection

The sample collection was performed separately for each of the data sets, and the Bayes classifier trained accordingly. The ice-radar image of Fig. 2(a) and the aerial photograph of Fig. 3 were compared, and sites corresponding to different ice types were located on the images. A simple rule of thumb for identifying an iceberg on the like-polarized image is to locate the shadow cast by it (Fig. 2(b)). It is observed in [11] that

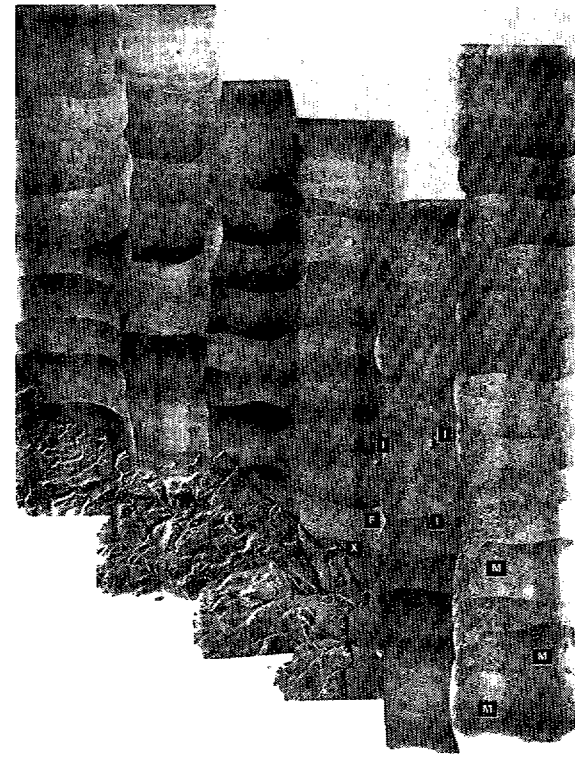

Fig. 3. Aerial photo mosaic: I = icebergs, M = multiyear ice, F = first-year ice, and X = camp location.

multiyear ice and icebergs depolarize the radar signal to a much larger extent than first-year ice. Hence, strong reflections are received from multiyear ice and icebergs, while feeble returns are received from first-year ice on the cross-polarized image. Regions corresponding to different ice types can be identified by comparing the like- and cross-polarized images obtained for the same radar. At least three different regions corresponding to an ice type were identified, and parameter estimation was performed for each of them separately. In some situations, the samples were combined, and the Bayes classifier was trained with the parameters estimated for the combined sample. In other situations, the classifier was trained with the parameters of the sample that produced the best classification results in terms of accuracy (to be described later).

B. Estimation of Unknown Density Parameters

The estimation of unknown density parameters can be divided into the following steps: identifying the shape of the density, estimating the unknown parameters, and performing a test of fit. We now address these issues one by one.

1. Identifying the Shape of the Density: The shape of the underlying density can be identified by first obtaining estimates of the first four sample moments, followed by the application of the Pearson rule for unimodal distributions.

Some families of distributions have been constructed by statisticians which are expected to provide approximations to a wide variety of observed distributions. The "Pearson System" is one such family, and was originated by Karl Pearson between 1890 and 1900 [12].

For every member of this system, the probability density

$f_X(x)$ satisfies the differential equation [12]

$$\frac{1}{f}\frac{df}{dx} = -\frac{(x+a)}{c_0 + c_1 x + c_2 x^2}.$$

The shape of the density depends on the parameters a, c_0, c_1, and c_2. Provided that a is not a root of the equation

$$c_0 + c_1 + c_2 x^2 = 0$$

the function f is finite when $x = a$, and $df/dx = 0$ when $x = -a$. Pearson classified the different shapes into a number of types. The solution of a, c_0, c_1, c_2 is obtained in terms of the first four moments μ_1', μ_2, μ_3, and μ_4 (μ_1' is the first moment about the origin and μ_2, μ_3, μ_4 are the second, third, and fourth moments about the mean). Define

$$\beta_1 = \frac{\mu_3^2}{\mu_2^3}$$

$$\beta_2 = \frac{\mu_4}{\mu_2^2}.$$

The "Pearson System" defined in terms of β_1 and β_2 is as follows [12]: If

$$k = \frac{1}{4} c_1^2 (c_0 c_2)^{-1}$$

$$= \frac{1}{4} \beta_1(\beta_2+3)^2(4\beta_2 - 3\beta_1)(2\beta_2 - 3\beta_1 - 6)^{-1}$$

then we may recognize the following special cases:

Normal	$\beta_1 = 0, \quad \beta_2 = 3$
Type I	$k < 1$
Type II	$\beta_1 = 0, \quad \beta_2 < 3$
Type III	$2\beta_2 - 3\beta_1 - 6 = 0$
Type IV	$0 < k < 1$
Type V	$k = 1$
Type VI	$k > 1$
Type VII	$\beta_1 = 0, \beta_2 > 3.$

Type I corresponds to the general form of the beta distribution. Type III corresponds to the general form of the gamma distribution. Type VII corresponds to the general form of the Student's t-distribution. Type II, Type IV, Type V, and Type VI do not conform to any known continuous distribution.

If $x_1, x_2, \cdots, x_n$ represent n independent samples of an ice type, the rth moment (m_r) about the mean is given by

$$m_r = \frac{1}{n}\sum_{i=1}^{n} (x_i - x^*)^r$$

where x^* is the sample mean defined by

$$x^* = \frac{1}{n}\sum_{i=1}^{n} x_i.$$

This estimate assumes that each of the n samples has a probability of $1/n$. The estimate of the sample skewness ($\sqrt{\beta_1}$) and kurtosis (β_2) are then given by

$$\sqrt{\beta_1^*} = \frac{m_3}{m_2^{3/2}}$$

and

$$\beta_2^* = \frac{m_4}{m_2^2}.$$

Using the estimated values of the skewness and kurtosis, the shapes of the sampling distributions of different ice types were determined. The distributions of all ice types were found to belong to the Type I family of distributions.

2. Estimating the Unknown Parameters: The method of moments was employed to estimate the parameters of the underlying sampling distributions. Although the method of maximum-likelihood is supposed to yield reliable estimates, it was not used because estimation of four parameters for the Type I distribution becomes rather complicated.

The general form of the density function for the Type I family of distributions is given by

$$f_Y(y) = \frac{(y-a)^{\alpha-1}(b-y)^{\beta-1}}{(b-a)^{\alpha+\beta-1}B(\alpha, \beta)}, \qquad a \le y \le b$$

where

$$B(\alpha, \beta) = \int_0^1 u^{\alpha-1}(1-u)^{\beta-1}\, du.$$

The four parameters, a, b, α, and β, have to be estimated; b and a correspond to the maximum and minimum values of the distributions, respectively. The maximum and minimum values of the samples were obtained, and these were used as the estimates for b and a. The sampling distribution was then transformed to

$$f_X(x) = \frac{x^{\alpha-1}(1-x)^{\beta-1}}{B(\alpha, \beta)}, \qquad 0 \le x \le 1$$

by assuming that $Y_{\max}^*$ occurs at $x = 1$ and $Y_{\min}^*$ occurs at $x = 0$. The values of x corresponding to the values of y were obtained by using the equation

$$x = (y-a)/(b-a).$$

Let $x_1, x_2, \cdots, x_n$ be random variables drawn from a population whose density function involves the unknown parameters $\theta_1, \theta_2, \cdots, \theta_k$. The moment estimators $\theta_1^*, \theta_2^*, \cdots, \theta_k^*$ of $\theta_1, \theta_2, \cdots, \theta_k$, respectively, are solutions of the system of simultaneous equations [13]:

$$m_r'(x_1, x_2, \cdots, x_n) = \mu_r'(\theta_1, \theta_2, \cdots, \theta_k), \qquad r = 1, 2, \cdots, k$$

where m_r' is the rth sample moment about the origin. It is given by

$$m_r' = \frac{1}{n}\sum_{i=1}^{n} x_i^r$$

and μ_r' is the rth moment of x about the origin obtained analytically. It is given by

$$\mu_r' = E(x^r) = \int_{-\infty}^{\infty} x^r f_X(x)\, dx$$

where $f_X(x)$ is a continuous density function.

The moment estimators for α and β for the Type I distribution were obtained as

$$\alpha^* = \frac{(1-m_1)m_1^2}{m_2} - m_1$$

and

$$\beta^* = \frac{\alpha^*}{m_1} - \alpha^*.$$

3. Performing a Test of Fit: The chi-square goodness-of-fit test was performed to determine the closeness between the estimated theoretical distribution and the observed sample histogram. To test the hypothesis that the sample does come from the estimated distribution, we form the statistic

$$\chi^2 = \sum_{1}^{k} \frac{(f_{0i} - nf_e(x))^2}{nf_e(x)} \tag{2}$$

under the condition that there are k intervals of values of x giving nonzero expected frequencies. The parameters in (2) are as follows:

- $nf_e(x)$ the expected frequencies,
- f_{0i} the observed frequencies,
- n the total number of samples.

As $n \to \infty$, the limiting distribution of (2) is chi-square ($k - 1$) [14].

The theoretical distribution is tested by comparing the values obtained in (2) with that of the value of chi-square ($k - 1$) obtained from the tables. The hypothesis is accepted if the value of the computed χ^2 is less than some critical value such as $\chi^2_{0.05,k-1}$, $\chi^2_{0.01,k-1}$, which are critical values at the 5- and 1-percent significance levels, respectively.

V. Implementation of the Classifier

Four spatial preprocessing operations were performed on the data. They were noise reduction, calibration, range normalization, and noise thresholding.

1. Noise Reduction: As radar images are not noise free, the images were first median filtered; the median filter order is 3 × 3. This filter has the effect of reducing the dispersion in the class densities and, hence, the region of indecision between classes.

2. Calibration: The digitized gray levels were converted to power by using a set of calibration points available for each radar.

3. Range Normalization: The normal free-space equation for power received from a point target (ignoring system losses) in a radar environment is given by

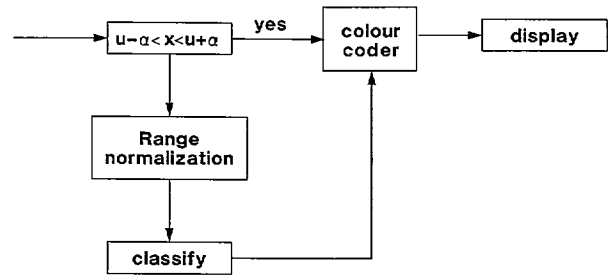

Fig. 4. Block diagram of noise-thresholding scheme.

$$P_r = P_t \frac{G^2 \lambda^2 \sigma_t}{(4\pi)^3 R^4} \tag{3}$$

where

- P_r received power (kilowatts),
- P_t transmitted power (kilowatts),
- G antenna gain,
- σ_t radar cross section of the target (square meters),
- λ radar wavelength (meters), and
- R range of the target (meters).

For a distributed target, the antenna beam illuminates the area of the target. Hence, the radar equation, (3), is modified to include the proximity of the target to the reflecting surface. Accordingly, P_r is given by

$$P_r = \frac{P_t G^2 \lambda^2 c\tau \theta_b \sigma_0 \sec\Psi}{2(4\pi)^3 R^3} \tag{4}$$

where

- θ_b antenna horizontal beamwidth (radians),
- Ψ grazing angle,
- c velocity of light (meters per second),
- τ pulse width (seconds), and
- σ_0 σ_t/area of target.

For small Ψ, we have $\sec\Psi \approx 1$. For the radars in question, Ψ is very small; hence, we may let $\sec\Psi \approx 1$. From (4), it is obvious that $P_r \times R^3$ should provide a scaled value of σ_0, the "reflectivity" of the target.

4. Noise Thresholding: Some of the images had to be thresholded for noise before any classification studies could be performed on them. The mean μ and variance σ^2 of the noise were determined. Samples lying within $\pm 2\sigma$ of the mean (μ) were eliminated from the study. These pixels were also bypassed by the classifier. Fig. 4 shows the block diagram of the scheme employed.

Sites corresponding to different ice types were located on the image using a digital tablet and a Ramtek 9460 Graphics Display system. The classification studies were performed separately for each data set. Table I gives the values of the estimated parameters for different ice types for each of the radar data. Fig. 5 shows a plot of the *a posteriori* probabilities $p(w_i|x)$ for the *Ku*- and *S*-band radar data, where $p(w_i|x)$ denotes the *a posteriori* probability that a pixel with feature vector x belongs to class w_i. Fig. 5(a) and (b) refers to like-

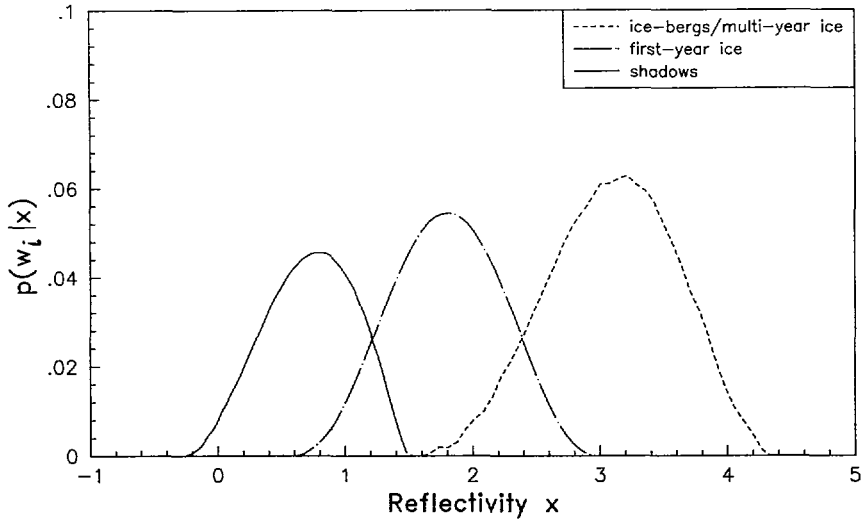

(a)

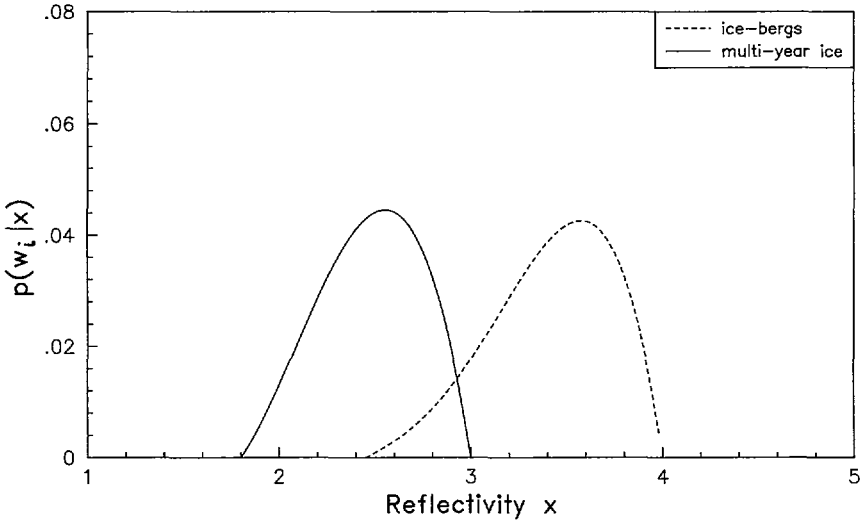

(b)

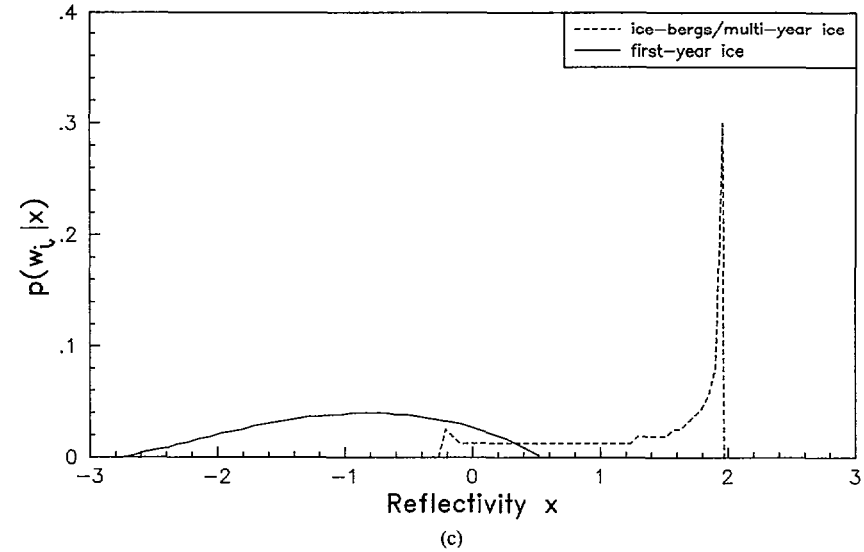

(c)

Fig. 5. (a) *A posteriori* probabilities for the *Ku*-band (like-polarized) data. (b) *A posteriori* probabilities for the *Ku*-band (cross-polarized) data. (c) *A posteriori* probabilities for the *S*-band (like-polarized) data.

TABLE I-A
PARAMETERS ESTIMATED FOR THE CLASS DENSITIES OF DIFFERENT ICE TYPES IN THE *Ku*-BAND LIKE-POLARIZED IMAGE

sample	moments of the sample				parameters of class disbn.					chi-square (n)	confidence level
type	μ_1	μ_2	Skewness	Kurtosis	shape	Y_{max}	Y_{min}	θ_1	θ_2		
First-year ice:											
(1)	1.45	0.081	0.62	4.21							
(2)	1.83	0.086	-0.11	2.48	I	3.0	0.47	4.1	3.9	13.35(10)	90%
(3)	1.62	0.13	-0.2	2.69							
(4)	2.18	0.12	-0.38	3.02							
Ice-bergs or multi-year ice:											
(1)	2.72	0.24	-1.53	4.96							
(2)	3.56	0.11	-0.38	2.89	I	4.48	1.03	5.9	4.2	9.75(6)	95%
(3)	3.06	0.073	-0.36	3.53							
Shadows:											
(1)	0.55	0.067	-0.47	3.22							
(2)	1.04	0.038	-0.19	3.12	I	1.46	-0.34	3.2	2.4	14.9(8)	95%
(3)	0.43	0.04	-0.37	3.06							

TABLE I-B
PARAMETERS ESTIMATED FOR THE CLASS DENSITIES OF DIFFERENT ICE TYPES IN THE *Ku*-BAND CROSS-POLARIZED IMAGE

sample	moments of the sample				parameters of class disbn.					chi-square (n)	confidence level
type	μ_1	μ_2	Skewness	Kurtosis	shape	Y_{max}	Y_{min}	θ_1	θ_2		
Multi-year ice:											
*(1)	2.46	0.06	-0.32	3.43	I	3.05	1.67	3.8	2.9	9.06(11)	90%
(2)	3.08	0.085	0.19	2.36	I	3.1	2.36	2.1	2.2	7.61(7)	95%
Ice-bergs:											
(1)	3.44	0.15	0.14	2.25	I	4.13	2.63	1.6	1.3	13.3(5)	reject
*(2)	3.35	0.13	-0.99	3.62	I	3.94	2.35	2.8	1.5	12.72(10)	90%
(3)	3.02	0.34	-0.41	2.51	I	4.04	1.55	1.9	1.4	22.5(9)	reject
(4)	3.8	0.31	-0.67	2.93	I	4.61	2.2	2.2	1.1	4.5(3)	90%
**Noise threshold:											
	55.6	56.4	(threshold 40.5 - 70.6)								

* Classifier trained with these parameters for the corresponding classes.
** The image was first thresholded to eliminate noise within $\pm 2\sigma$ of μ_1.

TABLE I-C
PARAMETERS ESTIMATED FOR THE CLASS DENSITIES OF DIFFERENT ICE TYPES IN THE *S*-BAND LIKE-POLARIZED IMAGE

sample	moments of the sample				parameters of class disbn.					chi-square (n)	confidence level
type	μ_1	μ_2	Skewness	Kurtosis	shape	Y_{max}	Y_{min}	θ_1	θ_2		
First-year ice:											
(1)	-0.71	0.15	0.16	2.67	I	0.24	-1.85	-0.71	0.15	8.4(11)	75%
*(2)	-0.93	0.5	-0.03	2.1	I	0.52	-2.92	2.5	2.0	14.84(9)	95%
(3)	-0.57	0.25	0.42	3.41	normal	0.9	-2.13	-0.53	0.25	81.3(30)	reject
Ice-bergs or multi-year ice:											
(1)	1.2	0.1	-2.24	6.61	I	1.41	0.2	1.7	0.55	4.8(2)	90%
*(2)	1.35	0.5	-0.85	2.17	I	1.96	-0.27	0.7	0.26	2.7(3)	75%
(3)	0.52	0.19	-0.55	2.52	I	1.27	-0.65	2.3	1.5	12.09	75%
**Noise threshold:											
	62.3	69.5	(threshold	45.6 - 78.9)							

* Classifier trained with these parameters for the corresponding classes.
** The image was first thresholded to eliminate noise within $\pm 2\sigma$ of μ_1.

polarized and cross-polarized *Ku*-band radar data, respectively. Fig. 5(c) refers to like-polarized *S*-band radar data.

VI. Classification Results

The classifier was trained with the density functions in Table I. The classification results are presented in Figs. 6–8. Figs. 6 and 7 show sections of the original *Ku*-band like- and cross-polarized images and the corresponding classification maps. Fig. 8 shows a section of the original *S*-band like-polarized image and its classification map.

An empirical approach has been employed to quantitatively measure the performance of the classifier. The classification was evaluated with respect to the training samples. Hence, the classification is biased (in the sense of Lachenbruch [15]). The performance was evaluated in the following way. Let

N_s = total number of sample points for an ice type

N_c = total number of sample points classified correctly.

Then, the classification accuracy is defined as

$$\text{accuracy} = \frac{N_c}{N_s}.$$

Table II gives the classification accuracies obtained for different ice types for all the images. It is observed that the classification accuracies obtained for the *Ku*-band data are significantly higher than those obtained for the *S*-band data. This is perhaps due to the poor range resolution of the *S*-band data.

TABLE II
PERFORMANCE OF THE BAYES CLASSIFIER

Performance of the Bayes' classifier(%)		
Ku-band radar(like-polarized) data:		
first-year ice	ice-bergs/multi year ice	shadows
82.9	75.7	96.9
Ku-band radar(cross-polarized) data:		
multi-year ice	ice-bergs	
52.1	67.5	
S-band radar(like-polarized) data:		
first-year ice	ice-bergs/multi-year ice	
96.6	52.7	

Postclassification Processing

To smooth out the boundaries between different ice types, all the classification maps were median filtered.

So far we have dealt with images in the *B*-scan format. The images were scan-converted to plan-position-indicator (PPI) format so that the location of different target classes with respect to the radar could be ascertained. Figs. 9 and 10 show the scan-converted classification maps of the *Ku*- and *S*-band data, respectively. In Fig. 9 we observe that icebergs have been identified on the like- and cross-polarized images at the same range and azimuth, although a lot of multiyear ice has

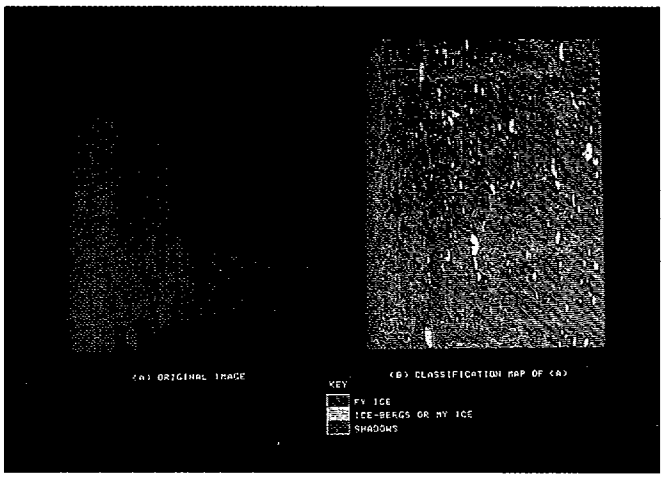

Figure 6

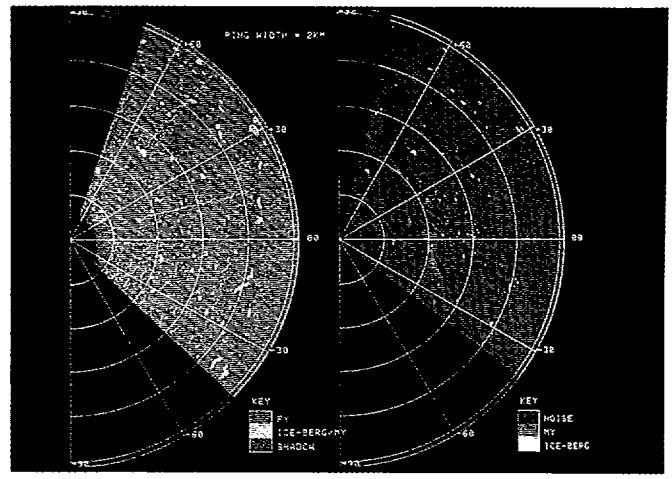

Figure 9

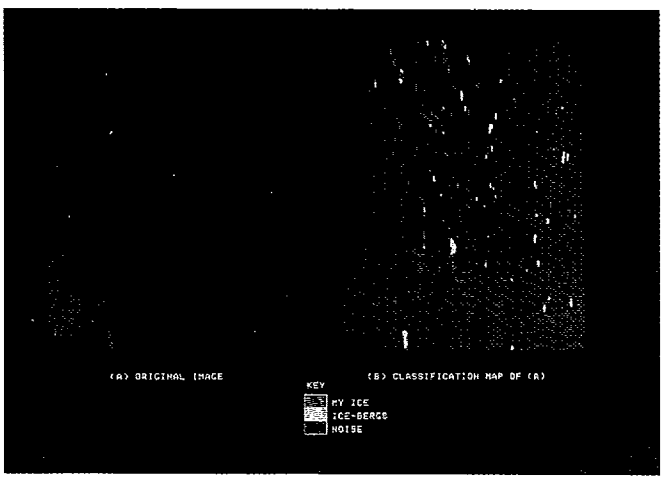

Figure 7

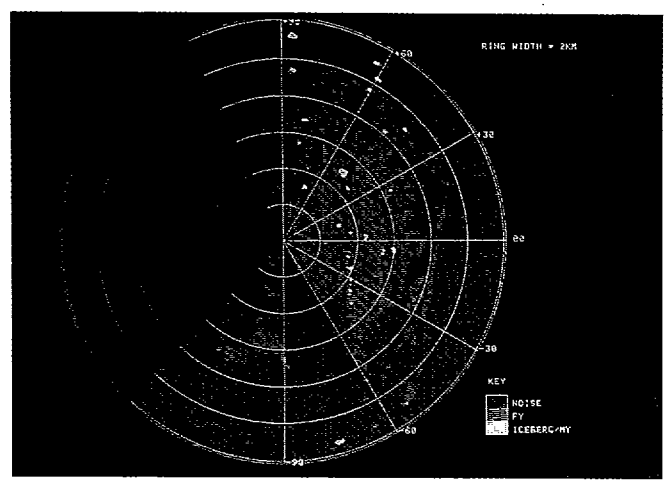

Figure 10

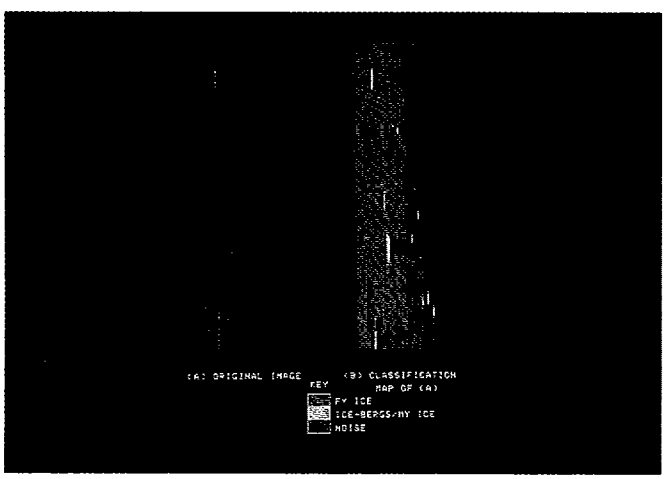

Figure 8

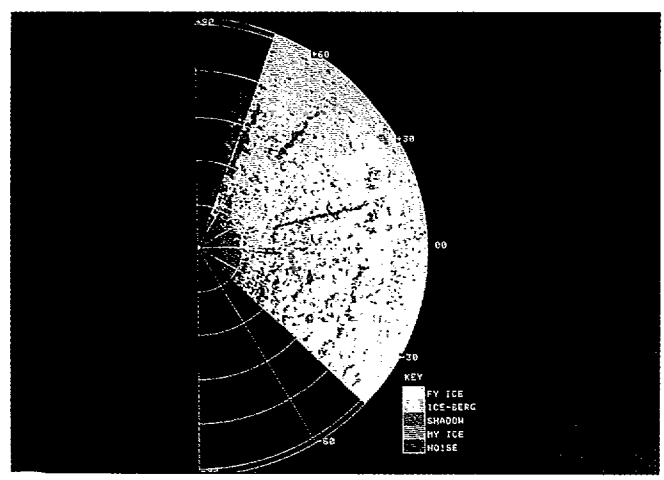

Figure 11

Fig. 6. Section of the original *Ku*-band like-polarized image and its classification map.

Fig. 7. Section of the original *Ku*-band cross-polarized image and its classification map.

Fig. 8. Section of the original *S*-band like-polarized image and its classification map.

Fig. 9. Scan-converted *Ku*-band classification maps.

Fig. 10. Scan-converted *S*-band classification map.

Fig. 11. Combined *Ku*-band classification map.

been classified as belonging to the iceberg class in the cross-polarized map.

A reduction in the probability of misclassification can be obtained by logically combining the two maps. An iceberg is always followed by a shadow in the like-polarized image. Hence, if a region corresponds to the iceberg or the multiyear ice class, and it is not followed by a shadow, the region may be assumed to correspond to the multiyear ice class rather than to the iceberg class. The distinction can be achieved by tracing the contours of the regions corresponding to either icebergs or multiyear ice. Once the contour is traced, a check is made to locate a shadow contour immediately following this region. If a shadow is not found, the region is classified as belonging to the multiyear ice class; otherwise, it is classified as an iceberg.

Finally, the cross-polarized classification map is combined with the modified like-polarized classification map to produce the result of Fig. 11. In this figure, the information about the different forms of ice is presented in such a way that we may readily distinguish between the regions of first-year ice, multiyear ice, and icebergs.

VII. Concluding Remarks

In this paper we have confirmed that ice, as seen by a surface-based marine radar, does exhibit considerable statistical variability. Hence, we may use decision-theoretic pattern recognition techniques to classify an ice field.

The Bayes procedure described in this paper is not the only way in which ice classification can be performed. The alternatives to this approach include 1) nonparametric classification techniques, and 2) multilevel thresholding. Although these procedures may not yield optimal classification results, nevertheless, they will consume significantly less computation time with not so significant a loss in classification accuracy. These two alternative approaches will be the subject of a future paper.

References

[1] V. H. Anderson, "High altitude side-looking radar images of sea-ice in the Arctic," presented at the 4th Int. Symp. Remote Sensing, Ann Arbor, MI, 1966.

[2] J. D. Johnson and L. D. Farmer, "Use of side-looking air-borne radar for sea-ice surveillance," *J. Geophys. Res.*, vol. 76, no. 9, pp. 2138–2155, Mar. 1971.

[3] A. Biache, C. A. Bay, and R. Bradie, "Remote sensing of the arctic ice environment," presented at the 7th Int. Symp. Remote Sensing, Ann Arbor, MI, 1971.

[4] R. D. Ketchum and S. G. Toome, "Analysis and interpretation of air-borne multi-frequency side-looking radar sea-ice imagery," *J. Geophys. Res.*, vol. 78, no. 3, pp. 520–538, Jan. 1973.

[5] M. Dunbar, "Interpretation of SLAR imagery of sea-ice in Nares strait and the Arctic ocean," *J. Glaciology,* vol. 15, pp. 193–213, 1975.

[6] W. F. Weeks, P. Sellman, and W. J. Campbell, "Interesting features of radar imagery of ice-covered North Slope Lakes," *J. Glaciology,* vol. 18, pp. 129–136, 1977.

[7] A. L. Gray, R. O. Ramseier, and W. J. Campbell, "Scatterometer and SLAR results obtained over arctic sea-ice and their relevances to the problems of arctic ice reconnaisance," presented at the 6th Canadian Symp. Remote Sensing, Quebec, Canada, 1977.

[8] R. T. Lowry, S. Schlien, and D. G. Goodenough, "A CCRS system of synthetic aperture radar imagery analyzer," presented at the 5th Canadian Symp. Remote Sensing," Victoria, B.C., Canada, 1978.

[9] R. T. Lowry and H. G. Hengeveld, "Optimizing imaging radar parameters for ice-reconnaissance," presented at the 6th Canadian Symp. Remote Sensing, Halifax, N.S., Canada, 1980.

[10] J. B. Mercer, R. T. Lowry, and S. K. Leung, "Experimental use of

real-time SAR imagery in support of oil exploration in the Beaufort Sea," presented at the 6th Canadian Symp. Remote Sensing, Halifax, N.S., Canada, 1980.
[11] S. Haykin, B. W. Currie, E. O. Lewis, and K. A. Nickerson, "Surface-based radar imaging of sea-ice," *Proc. IEEE,* vol. 73, pp. 233–251, Feb. 1985.
[12] N. L. Johnson and S. Kotz, *Continuous Univariable Distributions,* vols. 1 and 2. New York: Houghton Mifflin, 1970.
[13] J. K. Wani, *Probability and Statistical Inference.* New York: Appleton Century-Crofts, 1971.
[14] D. A. S. Fraser, *Probability and Statistics: Theory and Applications.* North Scituate, MA: Duxbury, 1976.
[15] P. A. Lachenbruch, *Discriminant Analysis.* New York: Hafner, 1976.

★

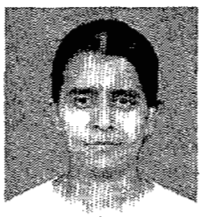

Hema A. Murthy received the B.E. degree from Osmania University, Hyderabad, India, in 1980, and the M.Eng. degree from McMaster University, Hamilton, Ont., Canada, in 1986.

From 1980 to 1983 she was a Scientific Officer in the Speech and Digital Systems Group of the Tata Institute of Fundamental Research, Bombay, India. During that time, she worked in the area of computer graphics. Since July 1986, she has been with the Department of Computer Science and Engineering, Indian Institute of Technology, Madras, India, pursuing the Doctorate degree. Her special interests are in the area of computer graphics, knowledge-based signal processing with applications to speech, image processing, and pattern recognition.

★

Simon Haykin (SM'70–F'82) received the B.Sc. degree (First-Class Honors), in 1953, the Ph.D. degree in 1956, and the D.Sc. degree in 1967, all in electrical engineering, from the University of Birmingham, Birmingham, England.

He is presently Director of the Communications Research Laboratory and Professor of Electrical and Computer Engineering at McMaster University, Hamilton, Ont., Canada. His research interests include image processing, adaptive filters, adaptive detection, and spectrum estimation with applications to radar.

Dr. Haykin is a Fellow of the Royal Society of Canada. He is corecipient of the Ross Medal from the Engineering Institute of Canada and of the J. J. Thomson Premium from the Institution of Electrical Engineers, London, England. He was awarded the McNaughton Gold Medal (IEEE, Region 7) in 1986.

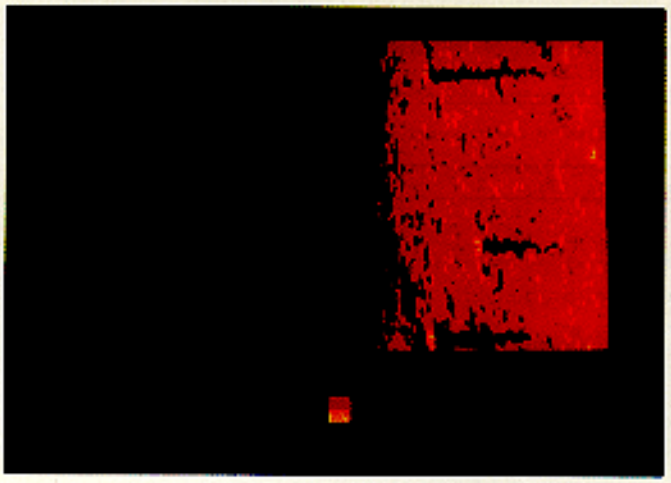

Figure 6

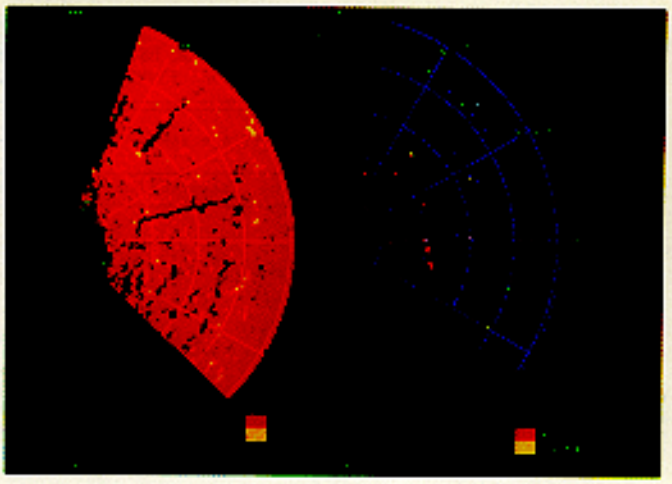

Figure 9

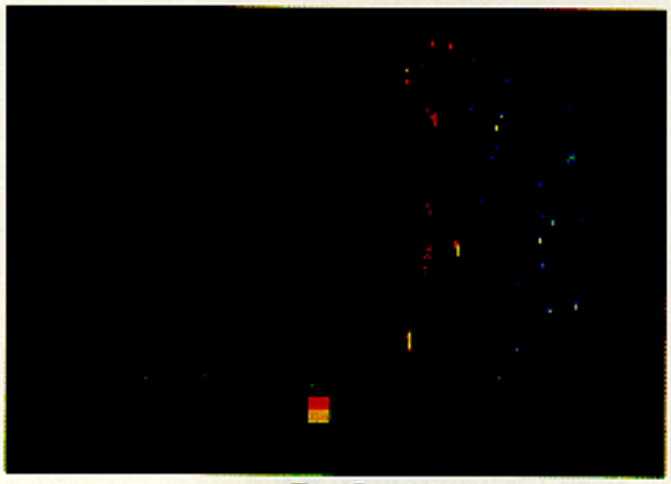

Figure 7

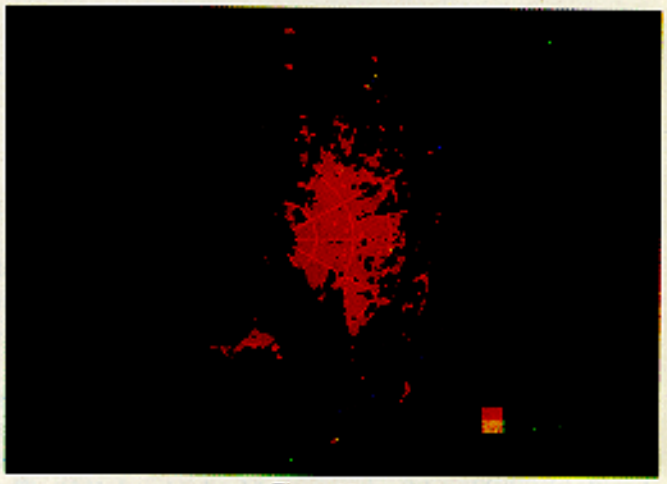

Figure 10

Figure 8

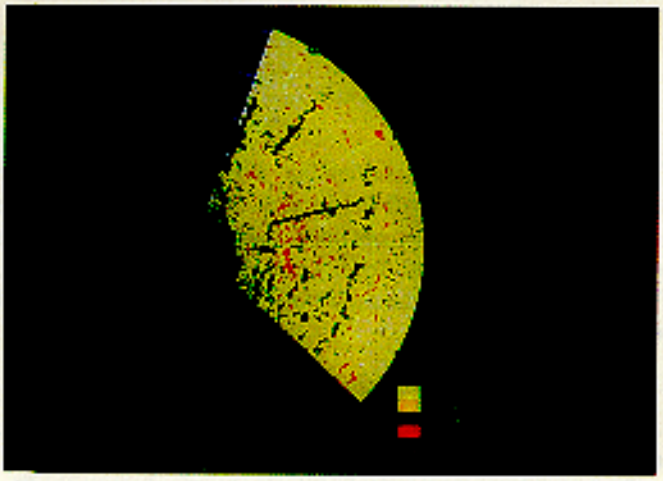

Figure 11